JOURNAL OF GEOPHYSICAL RESEARCH, VOL. 100, NO. E12, PAGES 26,345–26,355, DECEMBER 25, 1995

Compositional variations on the Moon: Recalibration of Galileo solid-state imaging data for the Orientale region and farside

Lisa R. Gaddis, Alfred S. McEwen, and Tammy L. Becker

U.S. Geological Survey, Flagstaff, Arizona

Abstract. Updated radiometric calibration and systematic processing procedures for Galileo solid-state imaging (SSI) data from the first (1990) Earth-Moon encounter are presented. These procedures were applied to a whole-disk imaging sequence of the Moon centered near Mare Orientale, called Lunmap 14 (L14). Processing of L14 data included radiometric calibration, subpixel coregistration, scattered light removal, geometric control and reprojection, photometric normalization, and calibration to Earth-based spectra. Coregistration and scattered-light removal procedures are improvements over the initial calibration of the SSI mosaics. The effects of scattered light correction are best seen using a whole-Moon view such as L14; resolution of the debated amounts of light scattering from within or outside the camera field of view is not necessary. Scattered light removal particularly affects the 1-μm spectral region and has implications for interpretation of mafic mineral signatures in mare deposits of the lunar limb and farside. Recalibrated spectra indicate that mare ponds of the limb show moderately deep 1-μm absorptions, and thus mafic mineral contents, comparable to those of other nearside basalts. Mafic mineral contents of Schiller-Shickard cryptomaria are higher than previously thought and are similar to some low-Ti nearside basalts. Many of the recalibrated spectra from South Pole/Aitken are similar to those of Schiller-Schickard cryptomaria, suggesting that many of these soils represent a mixed mare/highland lithology. The hypothesis that there is an olivine enrichment in southern South Pole/Aitken basin is not supported strongly by spectra shown here.

1. Introduction

The radiometric calibration and systematic processing procedures for Galileo solid-state imaging (SSI) multispectral data from the first Earth-Moon encounter (EM1; 1990) have been updated. Accurate calibration of these data is important for future interpretation of SSI data for Jupiter and the Galilean satellites, as well as for assistance in calibration of the new Clementine data for the Moon. Here the application of these updated procedures to Lunmap 14 (L14), a single whole-disk imaging sequence of the Moon centered near Mare Orientale (Figure 1), is described. L14 has a spatial resolution of ~8 km/pixel, a subspacecraft position of -20.7° latitude and 98.3° longitude, and was obtained at a 20° phase angle. SSI data were obtained with a charge-coupled detector (CCD) array through seven filters spanning the 0.4 to 1.0-μm wavelength range [e.g., *Belton et al.,* 1992]. Data from six of these filters were used in this analysis; data were obtained at nominal wavelengths of 410 (VLT), 560 (GRN), 660 (RED), 756, 889, and 990 (1-μm) nm (the poor-quality 727-nm data were not used).

L14 data provide an excellent example of the results of our recalibration procedures and of their effect on spectral analyses of the SSI data. A major element of the recalibration is the correction for scattered light, a low-intensity brightness component that is wavelength dependent and is approximately symmetric about the Moon in or near the field of view (FOV). At present, scattered-light correction is best seen in a whole-Moon view such as that of L14; distinction between possible amounts of light scattering from within or outside the FOV is not necessary. The results of these procedures and their implications for interpretation of the mafic mineral absorptions observed in spectra of (1) mare soils on the lunar limb and farside, (2) cryptomaria of the Schiller-Shickard region, and (3) the South Pole/Aitken Basin deposits on the lunar farside are discussed in this paper.

Paper number 95JE03102.

1.1. Data Processing

Systematic processing for the L14 imaging sequence has included (1) incorporation of updated calibration files from the Jet Propulsion Laboratory (JPL) into radiometric calibration procedures, (2) subpixel coregistration, (3) application of a scattered-light removal technique, (4) geometric control and reprojection, (5) photometric-function normalization, and (6) calibration to Earth-based spectral data. The subpixel coregistration and scattered-light removal procedures represent improvements over the initial calibration and processing of the Galileo SSI data as described by *McEwen et al.* [1993] (the reader is referred to this article for details on SSI data characteristics and processing requirements). These procedures and their effects are described in detail below in the order in which they were implemented on the L14 data.

1.1.1. Calibration. EM1 SSI images were acquired through a dust cover that resulted in reduced transmission, imaging of dust-related blemishes, and the production of ghost images (reflections). Klaasen and others at JPL have used both preflight calibration files acquired without a dust cover and inflight limb images of Venus to produce updated calibration files that include

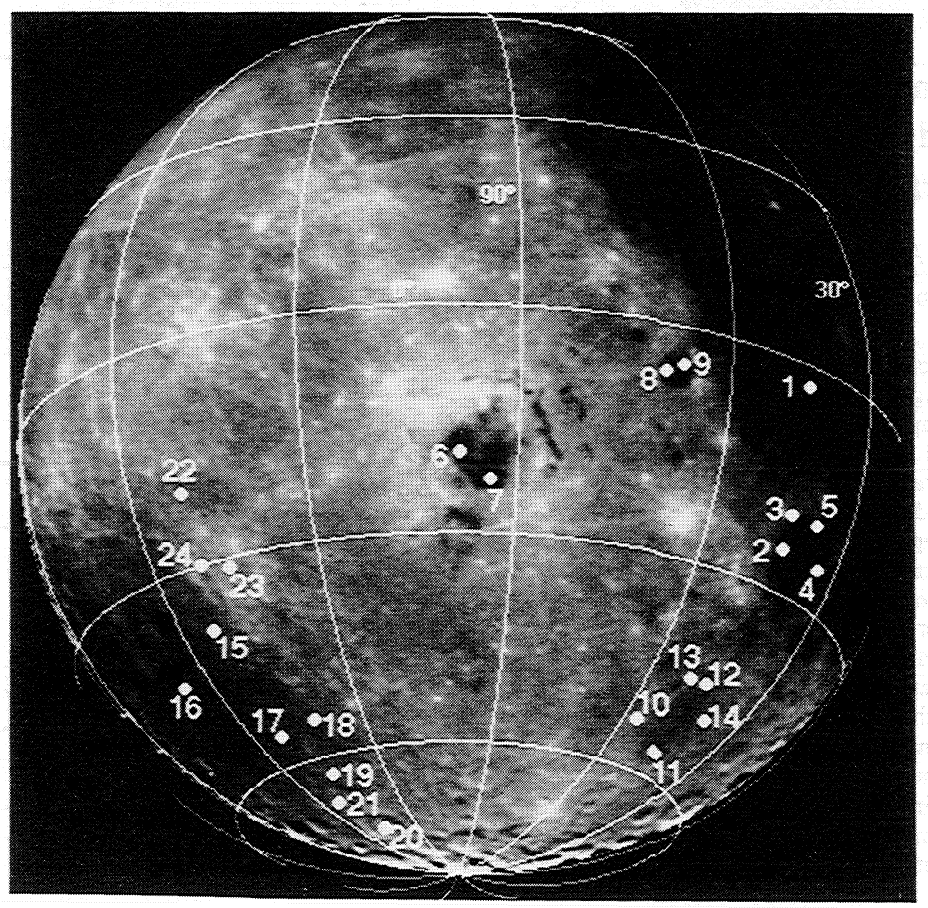

Figure 1. Albedo (0.560 μm, GRN filter) image of the L14 sequence. Dots mark the locations of spectral extractions used in the text; numbers correspond to entries in Table 2. The Orientale Basin (diameter 930 km; centered at 20°S, 95°W) is near the center of the Moon in this view.

corrections for dark-current, postlaunch shutter offset values (from Galileo's second Earth-Moon encounter, or EM2), nonuniformity in CCD sensitivity ("flat-fielding"), corner vignetting, and "donut" (dust ring) removal [e.g., *Klaasen,* 1993]. These calibration files (*Multimission Image Processing Subsystem,* 1994) are used here to perform radiometric calibration. The SSI ghost images, recognized as simple low-intensity reflections that are spatially offset from the primary body, are removed by multiplying each frame by the ratio of ghost brightness:primary image brightness, translating to accommodate the offset, and subtracting the resulting image from the original. For this analysis, ghost correction fractional values used during the original EM1 processing [*McEwen et al.*, 1993] were evaluated through analyses of residual brightness values of off-limb space and of the low-albedo mare deposit in Mare Grimaldi. After removal of residual ghosts in Mare Grimaldi, the original fractional correction values for the VLT (0.04), 889 (0.005), and 990 (0.03) filters required revision. Updated ghost correction fractional values from this analysis are VLT=0.043; GRN=0.004; RED=<0.002; 756=<0.002; 889=0.007; 990=0.025.

1.1.2. Subpixel coregistration. Pixel-to-pixel misregistration is a significant source of error in spectral analysis of highly correlated multispectral data sets [e.g., *McEwen et al.*, 1993]. We have developed software to resample images for coregistration to an accuracy of 0.2 pixel. For the L14 data, all images were coregistered to the base 756-filter image. The procedure includes selection of control-point values for evenly spaced subareas of the image to be coregistered; commonly 80 to 100 control points were used for L14 image pairs, each with a minimum correlation coefficient of 0.95. The subpixel coregistration software (distributed as a standard component of the USGS/PICS software [*Planetary Image Cartography System*, 1987]) uses polynomial least squares curve fitting to determine the best pixel brightness matches to within 1/5 pixel registration accuracy. Using the resulting spatial relationship, the image is geometrically transformed using nearest neighbor interpolation to warp or "rubber stretch" the image for coregistration. These techniques were applied to the EM1 L14 data, resulting in improved filter-to-filter registration and allowing more detailed spectral analyses near high-contrast boundaries.

1.1.3. Scattered-light correction. In addition to the dominant directly reflected light received by the SSI CCD detector, a low-intensity light component is observed in the SSI images of the Moon. This scattered light can be observed best as a dim halo next to the bright lunar limb [Belton et al., 1992]. As commonly discussed, the scattered light component may contain contributions from other bright objects in the vicinity of the imaged object ("veiling glare" [*Slater*, 1980]); light scattered inside the camera by dirt, edges, lens interfaces, etc.; and stray light that is captured by the camera from areas of the target outside the camera FOV [e.g., *Klaasen,* 1993]. In this paper we

distinguish between the effects of scattered light (resulting from internal scattering and glare) and those of stray light (light from beyond the FOV). The intensity of scattered light is wavelength dependent, with the highest amounts observed at 990, 889, 756, and VLT wavelengths (3% to 5% of the maximum signal at a distance of 25 pixels from the source, listed in decreasing order), and the least amounts observed at RED and GRN wavelengths (<3% of the maximum signal (*Klaasen*, 1993)]. The primary cause of the wavelength dependence of scattered light is due to the physical characteristics of the instrument; the lens cover, optical elements, inside of the telescope tube, etc. scatter light differently depending on its wavelength [K. Klaasen, personal communication, 1995].

Initial treatments of the EM1 data to minimize the color effects of scattered light required use of matched sets of images obtained through the same filter and imaging the same target, removal of regions of overlap with adjacent filter sets through masking of the margins of the filter sets, and empirical frame-to-frame brightness matching (after photometric normalization; see below) to normalize small residual offsets [related to phase-function residuals as well as scattered-light variations (*McEwen et al.*, 1993)]. However, these procedures did not determine a zero illumination level value (a value from shadows seen near the terminator of Lunmap 8 was used as the zero or dark-current level to establish a baseline value for spectral calibration), and they did not account for the different behavior of the scattered light at each wavelength.

In our updated processing to remove scattered light, we used a point-spread function (PSF) derived by K. Klaasen and A. Harch (both at JPL) for each filter (Figure 2). The function describes the attenuation of illumination (due to scattered light) on a single pixel as a function of distance from that pixel. The amount of scattered light expected for a given pixel is determined by multiplying the model attenuation factor for the pixel (at a desired distance) by the illumination at that pixel; contributions from all individual source pixels are summed to evaluate scattered light for an entire viewed image. The PSF was derived by constraining the scattered light near (0 to 2 pixels) and far from (>1000 to 10,000 pixels) the source pixel using prelaunch laboratory data (from knife-edge and navigation targets), and then iteratively modifying the central interpolated curve until it matched the observed scattered light. The resulting PSF predicts scattered light from a source pixel to within a factor of 2 of the scattered light observed in the laboratory for each filter [*Klaasen*, 1993]. To remove scattered light for a given filter, the Fourier transform of the attenuation function (i.e., the PSF for that filter) is convolved with the Fourier transform of the image at that wavelength and then filtered for noise removal in the frequency domain [e.g., *Cunningham and Anthony*, 1993]. To restore the sensor image that would have been present without scattered light, the resulting image then is transformed back to the spatial domain. Use of inflight scattered-light data from Galileo EM2 should permit refinement of these PSFs.

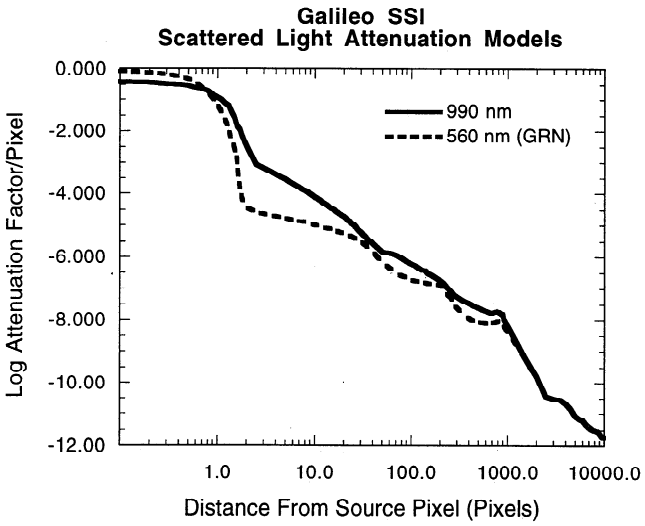

Figure 2. Plot of the point spread functions for two SSI filters (990 and GRN). In the SSI lunar data, the largest amount of attenuation due to scattered light is observed in the 990-filter data and the least amount is observed in the GRN-filter data. For a given wavelength, this function describes attenuation of illumination on a single-source pixel due to scattered light (shown as the logarithm, or 10^{-n}, of the attenuation factor n in inverse steradians) in the 990-nm and 560-nm Galileo SSI filters [figure after *Klaasen* [1993]). To determine the scattered light expected for a single pixel, multiply the attenuation factor for the pixel (at a desired distance) by the illumination at that pixel. For evaluation of scattered light for an entire image, contributions from individual source pixels are summed over the whole image.

The scattered-light attenuation model does not distinguish between light scattering sources within or outside the FOV of the detector, i.e., between scattered light and stray light. In the case of the whole-disk L14 data, it is not necessary to make this distinction. However, we found that removal of scattered light from sequences of partial-disk images prior to mosaicking does not adequately account for the observed image brightness offsets. We interpret the resulting low-frequency brightness discrepancies to be largely due to stray light. For partial-disk image sequences (i.e., most of the lunar Galileo SSI data), effective removal of scattered light will require the development of separate models for sources within and outside the FOV.

Although stray light (when present) contributes to a general brightening of an image, the effects of scattered light can be viewed as an overall redistribution of light within an image, resulting in a blurring of the image near high-contrast boundaries. To the extent that differences in image contrast are wavelength dependent, the apparent effects of scattered-light removal are expected to be different for different SSI filters. An image with zero contrast at a given wavelength would show no evidence of scattered light because the light scattered out of a given pixel would be entirely balanced by light scattered into that pixel from others (K. Klaasen, personal communication, 1995). Scattered light is expected to be most prominent at the lunar terminator and limb, because contrast is highest in those areas, and at high-contrast albedo boundaries where contamination of the low-albedo spectral response by the scattered light from high-albedo surfaces might occur (and vice versa, but to a relatively lesser extent). Removal of scattered light increases image contrast and thus results in brighter limbs and blacker space and, away from limb regions, darker low-albedo areas and brighter high-albedo areas. For example, for the L14 data with correction for scattered light, we observe brightness differences between scattered-light uncorrected and corrected data for the mare deposit within Crater Grimaldi (ENE of Orientale Basin); these differences are as much as 5% darker for the 990 nm data, 1% for the 756 and GRN data, and 0.6% or less for the VLT, 889, and RED data. For a highlands area northeast of Orientale, we observe differences of ~3% for 990, 889, and 756 data, 2% for VLT and RED, and ~1% for GRN filters. As discussed below, this result implies that scattered light is indeed significant near high-contrast boundaries;

spectral signatures of small mare deposits within the lunar highlands may be artificially brighter due to scattered light. Following ghost removal, correction for scattered light normalizes space to within 5 DN of zero (~0.5% of the maximum signal).

1.1.4. Geometric control and reprojection. To enhance comparison of spectral units with surface morphology, geometric control of L14 was established through use of the unified lunar control net [*Davies et al.*, 1987, 1994]. Tie points to the control points and match points between SSI frames were used to correct camera angles. An orthographic projection was used to display L14 data, and as a visual aid, control points were displayed on USGS shaded relief maps [*U.S. Geological Survey*, 1980, 1981, 1992].

1.1.5. Photometric-function normalization. For valid comparison of lunar surface properties (e.g., composition, particle size), the illumination and viewing geometry of the L14 data must be corrected to common values. The desired value to be derived is the normal albedo, or the reflectance of a surface when viewed normally (i.e., along the surface normal) at zero phase angle (i.e., full moon) relative to an ideal white diffusing surface. Modeling of normal albedo was accomplished for initial EM1 data analyses through the application of the Hapke photometric-function parameters derived for disk-integrated lunar observations by *Helfenstein and Veverka* [1987]. It was determined from examination of normalized EM1 images that these parameters (single scattering albedo w=0.21, regolith compaction parameter h=0.07, opposition surge amplitude S=0.71, asymmetry factor of the particle phase function g=-0.1, and macroscopic roughness parameter θ=20°, applied to all filters) provided adequate limb-darkening correction for most areas, but they overcorrected the image brightnesses at high photometric latitudes (which are also high geographic latitudes for EM1 observations [*McEwen et al.*, 1993]). This overcorrection inadequately normalized the limb darkening at high latitudes and at higher phase angles, thus directly affecting the mapping of normal albedo and indirectly affecting color ratios by biasing the brightness matching between frames. Empirically reducing the roughness parameter (θ) from 20° (the disk-integrated lunar value) to 5° (and applying it to each L14 whole-disk image) eliminated this problem and provided an adequate limb-darkening correction.

1.1.6. Calibration to Earth-based data. Spectral calibration of the L14 data requires the use of relative reflectance spectra from Earth-based telescopes and from samples of mature soils [*Pieters et al.*, 1993]. Neither of the standard lunar areas normally used for calibration (the Apollo 16 site in the central lunar highlands and the MS2 site in Mare Serenitatis) were illuminated during the Galileo flyby. Instead, a secondary standard area in Mare Humorum (MH0; -20.5° latitude, 37.4° longitude) has well-known characteristics relative to MS2 and Apollo 16 and was used to calibrate the L14 data. Reflectance spectra relative to MH0 (SSI/MH0) were obtained by scaling data in each band to the value of MH0 in that band. These spectra

Table 1. Reflectance Values Used for Calibration of L14 Data to Earth-Based Data

Filter	MH0/MS2	MH0/Sun
VLT	1.0464	0.05797
GRN	1.0007	0.07175
RED	0.98837	0.08075
756	0.98261	0.08811
889	0.97966	0.08949
990	0.97002	0.09126

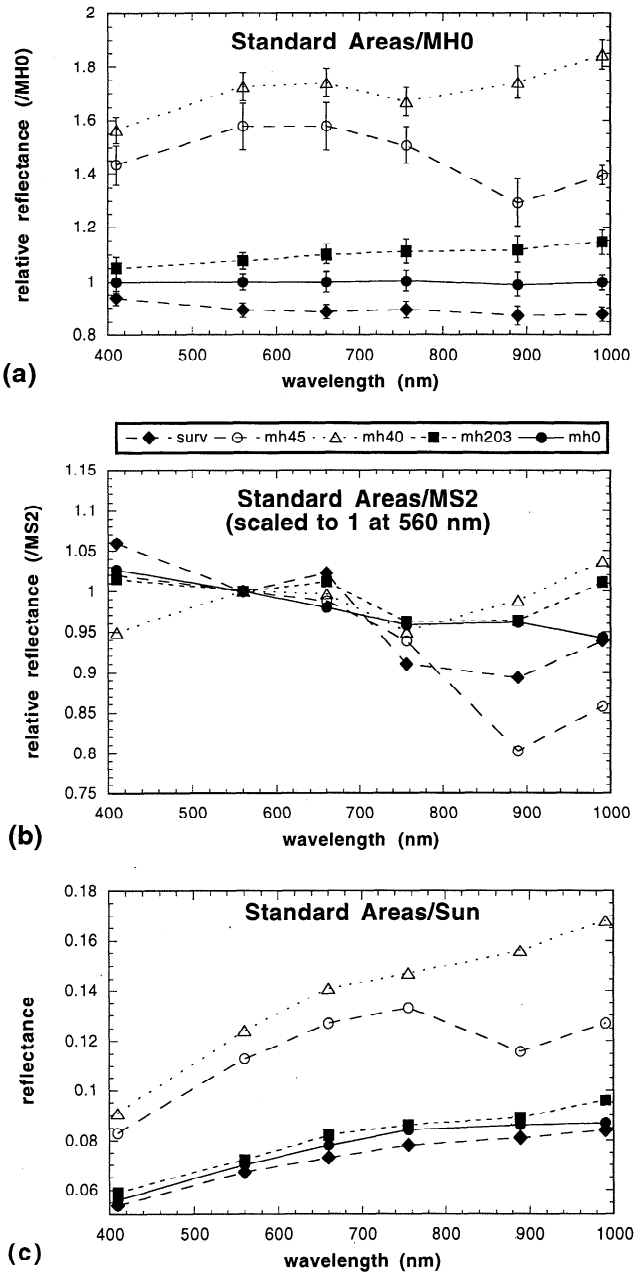

Figure 3. Reflectance spectra extracted from L14 (see Table 2 for site locations) for five standard areas on the western lunar nearside. Wavelength is in nanometers (1000 nm = 1 μm): "surv" is from the dark basalts of the Flamsteed ring in Oceanus Procellarum, "mh45" is a fresh mare crater in Mare Humorum, "mh40" is a highland soil north of Mare Humorum, "mh203" is a mare soil from southeast Mare Humorum, and "mh0" is the mare soil in northern Mare Humorum, MH0. For this work, MH0 serves as a secondary calibration standard, relative to Apollo 16 and MS2. Spectra are shown as (a) reflectance relative to MH0, (b) reflectance relative to MS2 (scaled to 1 at 560 nm), and (c) "absolute" reflectance (relative to Sun). Error bars in Figure 3a are the standard deviation of the statistical average of the group of pixels measured for each site; pixel to pixel variance is of the order of 6% or less. See *Pieters et al.* [1993] for a more detailed discussion of errors in the SSI data.

show color variations relative to the MH0 mare area as well as albedo differences between areas. For comparison to many published lunar spectra and multispectral images from previous analyses of telescopic and orbital data [e.g., *Greeley et al.*, 1993; *McEwen et al.*, 1993; *Pieters et al.*, 1993], L14 data are also presented as spectra relative to MS2 using Earth-based spectral information about MH0/MS2 values. Spectra and band-ratio images derived from SSI data relative to MS2 provided the primary information used for evaluation of the validity of our procedures and their effects on science analyses. Finally, spectra calibrated to solar reflectance (SSI/Sun) are also presented; derivation of these "absolutely" calibrated data are described by *Pieters et al.* [1993] as follows:

$$SSI_x/Sun=[(SSI_x/MH0)(MH0/Ap16)_{sc.tele.}(Ap16/Sun)_{Lab}]0.5.$$

Table 1 shows the reflectance values that were used to calibrate the SSI spectral data (revised from *Pieters et al.* [1993] by C.M. Pieters (personal communication, 1994)). Reflectance values for the SSI data are obtained by multiplying the following parameters: SSI/MH0 data; telescopic values of MH0/Apollo 16 (scaled to 0.56 μm); calibrated laboratory measurement of the Apollo 16 soil (obtained at a 20° phase angle); and a scaling factor (0.5) to account for the difference in albedo between Apollo 16 and MH0 [i.e., a factor of 2 [*Pohn and Wildey*, 1970]). Such SSI/Sun spectra preserve relative albedo information.

To corroborate our Earth-based calibration of L14, spectra were extracted for several standard areas on the western lunar nearside (Figure 3); these areas represent a variety of surface lithologies with well known spectral characteristics. Table 2 lists the image locations and sample sizes of these and other spectra presented here. These standard areas correspond as closely as possible to those used as standards by *Pieters et al.* [1993]. For these and other spectra presented in this paper, primary emphasis will be placed on interpretation of two major reflectance properties relative to the MS2 standard mare area: the ratio of the blue to the visible filters (i.e., the UV/VIS ratio or 0.40/0.56 μm), and on strength of the 1-μm mafic absorption band (0.76/0.990 μm). As described by *Pieters et al.* [1993, and references cited therein], the UV/VIS ratio is empirically related to the TiO_2 content of mature lunar mare soils: high-Ti ("blue") soils have an estimated TiO_2 content of >6 wt %, medium-high-Ti soils are 3 to 7 wt %, medium-Ti soils are <4 wt %, and low-Ti ("red") soils have <2 wt %. Overlap between these categories reflects uncertainties in the empirical relationship; greater uncertainties exist for units with intermediate TiO_2 content [e.g., *Pieters et al.*, 1993]. The depth of the 1-μm absorption band is related directly to the mafic mineral content of mature mare soils [see *Pieters et al.*, 1993 and references therein].

Three mare soils are included among the standard areas: mh0 is a "blue," medium high-Ti (medium-high UV/VIS) mare soil from northern Mare Humorum; surv is a low-albedo, "blue", high-Ti (high UV/VIS) mare soil from the Flamsteed ring of Oceanus Procellarum; and mh203 is a "blue," medium-Ti (low UV/VIS) soil from Mare Humorum. The cited color (relative albedo), UV/VIS, and mafic mineral characteristics are best seen in Figures 3a and 3b, which show reflectance of the standard areas relative to MH0 (Figure 3a) and to MS2 (Figure 3b, scaled to 1 at 560 nm). For comparison, the highland soil (mh40) has a

Table 2. Locations of L14 Spectra

Site	Name	Unit*	Upper Left		Lower Right		Number of Lines	Number of Samples
			Lat-itude	Long-itude	Lat-itude	Long-itude		
1	surv	mm	-2.2	43.6	-2.8	42.3	5	4
2	mh45	fc	-24.7	45.4	-25.0	44.7	3	2
3	mh40	h	-19.7	44.5	-20.4	44.2	4	1
4	mh203	mm	-24.5	33.5	-25.5	32.5	6	7
5	mh0	mm	-20.5	37.8	-20.8	35.4	5	5
6	15mor	mm	-18.6	98.5	-18.8	98.2	2	2
7	12mor	mm	-23.2	93.4	-23.4	93.1	2	2
8	87mgr	mm	-6.9	69.4	-7.1	69.1	2	2
9	7mgr	mm	-5.8	67.7	-6.3	67.4	3	2
10	74ssh	fc	-51.6	57.6	-52.1	56.6	3	2
11	32ssh	ip	-54.9	44.4	-56.5	43.4	6	8
12	30ssh	ip	-45.3	46.2	-47.1	43.6	9	2
13	29ssh	ip	-45.3	48.9	-46.7	47.1	7	2
14	28ssh	ip	-47.4	40.6	-48.9	37.8	8	2
15	33spa	cb	-37.7	143.5	-41.5	138.5	11	19
16	34spa	cb	-45.9	154.8	-48.9	151.3	8	4
17	35spa	cb	-54.8	142.5	-58.5	138.6	10	16
18	36spa	cb	-53.2	132.6	-56.7	130.2	11	12
19	39spa	sh	-62.5	135.4	-66.5	131.3	10	15
20	40spa	sh	-73.6	135.6	-76.8	132.5	17	11
21	41spa	sh	-67.1	144.0	-70.3	140.5	7	13
22	53spa	nh	-20.7	140.3	-23.2	138.3	9	9
23	54spa	nh	-29.8	136.0	-32.4	133.6	9	11
24	84spa	nh	-29.3	144.6	-30.8	143.8	6	5

* mm, mature mare soil; fc, fresh crater; h, lunar highland soil; ip, intercrater plains; South Pole/Aitken Basin (spa) soils: cb, central basin; sh, southern highlands; nh, northeastern highlands.

high albedo, low UV/VIS, and very little or no mafic mineral absorption (very low 0.756/0.990 μm). By contrast, the mare crater (mh45) is slightly less bright, has a low UV/VIS, and shows a strong mafic (pyroxene) mineral absorption (high 0.756/0.990 μm), even stronger than those of mare basalts in Mare Humorum (mh203) and southern Oceanus Procellarum (surv).

These analyses of spectra from standard areas (Figure 3) are in general agreement with those of *Pieters et al.* [1993] for the same or similar standard areas. However, recalibrated spectra for MH45 do not show as strong a 1-μm absorption as that observed by *Pieters et al.* [1993]. This may be due in part to the larger pixel sizing of the L14 data: L14 pixels are approximately twice that of the Lunmap 8 data from which the *Pieters et al.* [1993] data were extracted. Our spectrum for this small feature may be weakened by inclusion of adjacent mature mare deposits in the spectrum; this possibility is supported by the slightly lower UV/VIS ratio that is also observed in the recalibrated spectrum for this deposit (the UV/VIS values for the crater MH45 and the Mare Humorum basalt MH203 are very similar in the recalibrated data).

1.2. Summary of Spectral Effects of Recalibration

In the recalibration of the L14 data described here, the removal of scattered light has the most significant effect on the spectral properties of the SSI data. To examine the spectral effects of scattered light removal, we looked at the Lunmap 14 images for all filters before and after correction. As an example of a typical highlands region, data for an area NE of Orientale basin are about 3% brighter after scattered light removal for the 990, 889, and 756 filters, about 2% brighter for the RED and VLT filters, and about 1% brighter for the GRN filter. A mare pond in the highlands (such as Mare Grimaldi) is about 5% darker for the 990 data, about 1% darker for the 756 and GRN data, and less than 1% darker for the 889, RED, and VLT data. The calibration standard area in Mare Humorum is about 2% darker for the 990 filter after scattered-light removal, and for the GRN filter it is about 1% darker; for 889, 756, RED, and VLT data there was virtually no change in brightness. Because the change in VLT and GRN is 1% or less for both mare ponds and the MH0 standard, we expect little or no change in the recalibrated data for the UV/VIS ratios for units in these areas. However, the combined effect of a 1% or less change in 756 and the 3% difference in the 990 data for small mare ponds and MH0 suggests that there will be an overall increase in the 1-μm band depth of about 3% for such deposits. Reflectances of high-albedo features (such as highlands deposits and impact craters) relative to MH0 at 990, 889, and 756 filters show an average 5% increase in brightness, and at VLT, GRN, and RED filters, there is a ~2% brightness increase. The GRN/990 ratio, used as a soil maturity index for crater dating [e.g., *Johnson et al.*, 1991; *McEwen et al.*, 1993], is expected to be ~3% higher. These examples illustrate the approximate magnitudes of the color changes observed in the lunar limb deposits following recalibration, particularly scattered-light removal, of the L14 SSI data. As described above, the amount of scattered light (and thus the amount removed) occurring for any given unit will vary with the local spectral contrast. In the following section, we will focus on the effects of scattered-light removal on the compositional interpretation of several mafic deposits in the Lunmap 14 data.

2. Results and Discussion

The results of the recalibration procedures presented above, especially the removal of scattered light from the L14 data, have implications for interpretation of several major science issues previously addressed with the Galileo SSI data, three of which will be discussed here: (1) the weak or nonexistent mafic mineral (1-μm) absorption previously observed in spectra of many limb and farside mature soils on small mare deposits [e.g., *Greeley et al.*, 1993; *Pieters et al.*, 1993]; (2) the mafic mineral absorptions of cryptomare deposits near Schiller-Schickard [e.g., *Pieters et al.*, 1993; *Greeley et al.*, 1993]; and (3) the farside mafic anomaly at South Pole/Aitken Basin [e.g., *Davis and Spudis*, 1987; *Belton et al.*, 1992; *Head et al.*, 1993; *Pieters et al.*, 1993; *Lucey et al.*, 1995].

2.1. Small Maria

The weak or nonexistent 1-μm absorption features of spectra from many mare ponds on the western limb and lunar farside were interpreted to indicate a very low mafic mineral content for these mare deposits [e.g., *Pieters et al.*, 1993; *Greeley et al.*, 1993]. The reported low mafic mineral content is unusual for the major mare lithologies of nearside basalts, and it suggested an inherently different lithology for the limb basalts. Two small mare deposits from Mare Orientale (15mor and 12mor) and two

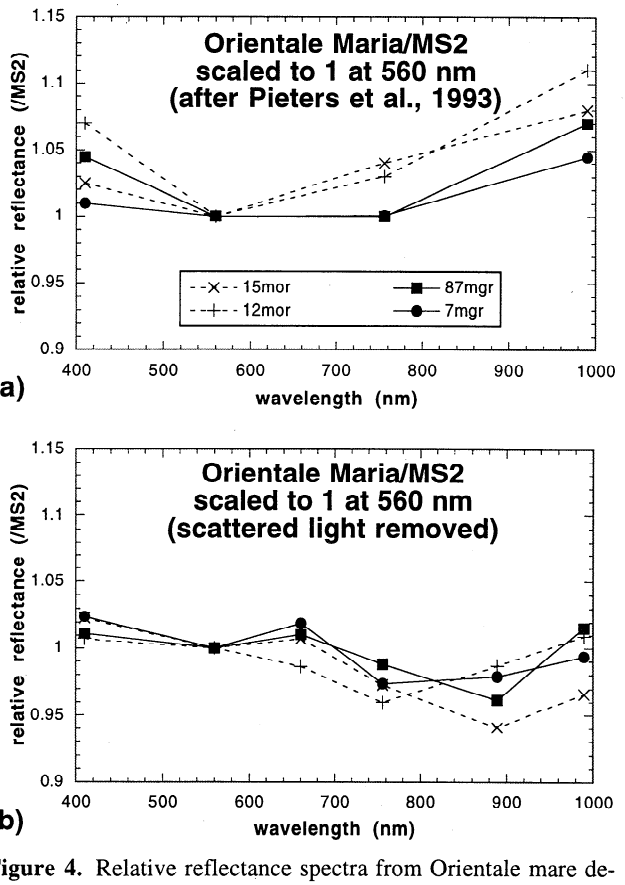

Figure 4. Relative reflectance spectra from Orientale mare deposits (see Figure 1 and Table 2 for site locations). (a) Spectra from the previous data calibration [after *Pieters et al.*, 1993]; (b) spectra after recalibration and scattered-light removal. Spectra are scaled to 1 at 560 nm.

from Mare Grimaldi (87mgr and 7mgr) are shown in Figure 4. In the previously calibrated data (Figure 4a), the Orientale mare ponds show no appreciable 1-μm absorption features. However, following removal of scattered light, spectra from the same areas show moderately deep 1-μm absorption bands (Figure 4b). Specifically, the relative reflectance values at 990 nm decrease in all sample spectra: there is a 10% change for 15mor, an 8% change for 12mor, and ~5% changes for 87mgr and 7mgr. Comparison of the 1-μm band depths of the recalibrated spectra to those of the standard areas shown in Figure 3b indicates that the mafic contents of these limb basalts are comparable to those of other nearside basalts (e.g., mh203). Also note that, in agreement with previous results [e.g., *Pieters et al.*, 1993; *Greeley et al.*, 1993], the UV/VIS ratios of the Orientale maria are still medium to medium-high, indicating that these mare deposits have intermediate titanium contents (medium-high~0.97 to 1.02, high~1.02 to 1.07 [*Pieters et al.*, 1993]).

2.2. Cryptomaria

Cryptomaria are thought to be mare deposits that have been covered by younger highland ejecta [e.g., *Hawke and Bell*, 1981; *Schultz and Spudis*, 1979]. Cryptomare spectra exhibit the moderate to low albedos and moderately strong 1-μm band depths expected from a mixture of highland and mare lithologies.

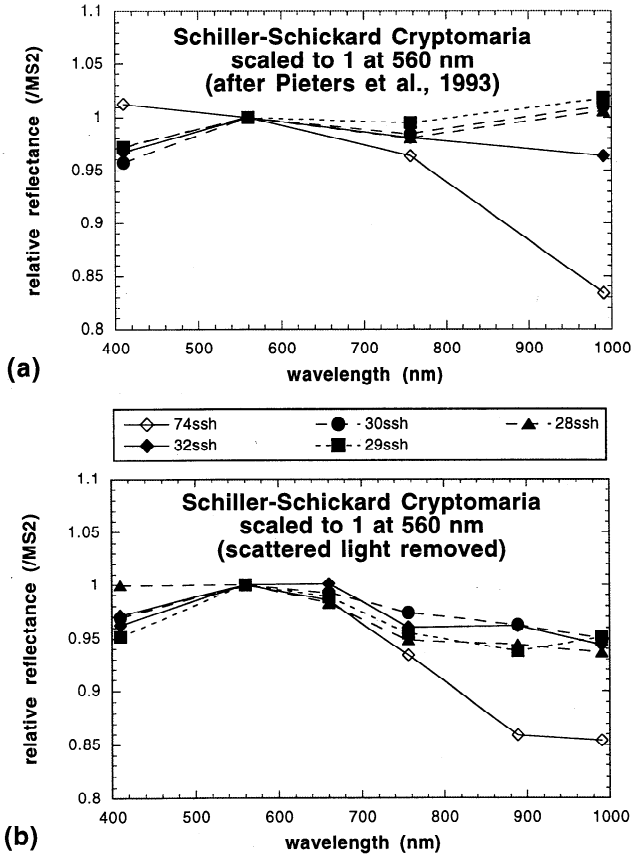

Figure 5. Relative reflectance spectra from the cryptomare deposits of the Schiller-Schickard region (see Figure 1 and Table 2 for site locations). (a) Spectra from the previous data calibration [after *Pieters et al.*, 1993]; (b) spectra after recalibration and scattered-light removal. Spectra are scaled to 1 at 560 nm.

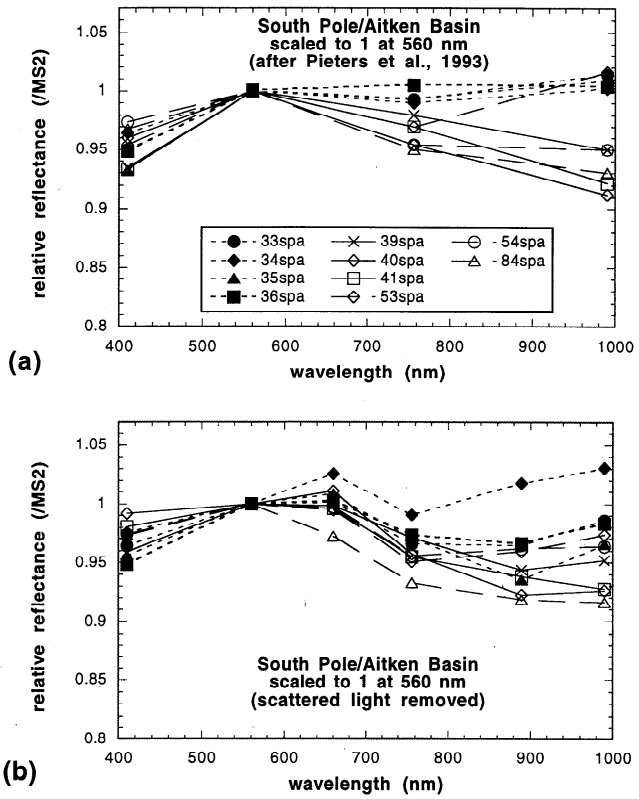

Figure 6. Relative reflectance spectra from the South Pole/Aitken Basin (SPA) region (see Figure 1 and Table 2 for site locations). (a) Spectra from the previous data calibration [after *Pieters et al.*, 1993]; (b) spectra after recalibration and scattered-light removal. Spectra are scaled to 1 at 560 nm.

Spectra from cryptomaria of the Schiller-Schickard area, southeast of Mare Orientale, were examined in this study (Figure 5). All spectra in Figure 5 except for 74ssh are from the low-albedo cryptomare deposits; for comparison, 74ssh is a local fresh crater with a very strong 1-μm absorption, suggesting that it has exposed fresh mare basalt. In the recalibrated spectra (Figure 5b), low UV/VIS values (indicative of intermediate Ti contents) comparable to those in the previously calibrated spectra (Figure 5a, after *Pieters et al.*, 1993] are observed, but the 1-μm band depths are again greater for the spectra from which scattered light has been removed. The relative reflectance values at 990 nm decrease in all sample spectra except one: there is a ~1% increase for 74ssh (a fresh crater), a 1% decrease for 32ssh, and ~5% decreases for 30ssh, 29ssh, and 28ssh. The 1-μm band depths in the recalibrated data are now comparable in strength to some of the low-Ti nearside basalts (such as mh0, Figure 3). These spectra, with the combined 1-μm band depths and low UV/VIS values, support the previous interpretations of *Head et al.* [1993] and others [e.g., *Hawke and Bell*, 1981; *Schultz and Spudis*, 1979; *Mustard et al.*, 1992] that mafic deposits underlie probable highland ejecta units in the Schiller-Schickard region.

2.3. South Pole/Aitken Basin

Belton et al. [1992] identified a major anomaly in the SSI data for the southern lunar farside. These authors attributed the presence of this low-albedo anomaly, associated with the South

Pole/Aitken Basin region (SPA, diameter 2200 to 2500 km (*Stuart-Alexander*, 1978; *Wilhelms et al.,* 1979; *Wilhelms*, 1987]), to an enhancement of mafic minerals in the highlands materials within the basin [*Belton et al.*, 1992]. This idea is supported by an increase in iron content in northern SPA detected by Apollo 15 gamma ray measurements [e.g., *Davis,* 1980]. Although more than 35 small mare patches have been mapped within the inferred inner ring (2000-2200 km diameter) of the South Pole/Aitken Basin (many are mare ponds inside the younger impact craters and basins, such as Apollo, Ingenii, Leibnitz [*Wilhelms et al.*, 1979]), the low-albedo area is more areally extensive. Topographic data [*Zuber et al.*, 1994] and the large size of this mafic-mineral enhancement suggest that the SPA was formed by an impactor that penetrated the lunar crust and excavated mafic materials from the lunar mantle [*Belton et al.*, 1992; *Pieters et al.*, 1993; *Head et al.*, 1993].

As observed on the recalibrated L14 image (Figure 1), the low-albedo SPA feature is ~2000 km in diameter and is centered at about -40° latitude, 170°W longitude. Figure 6 shows spectra from the SPA region from the previous calibration [after *Pieters et al.*, 1993] after removal of scattered light. On Figure 6, the four spectra marked with solid symbols (33spa, 34spa, 35spa, and 36spa) are from the low-albedo deposits in the basin interior; the three spectra marked with solid lines (39spa, 40spa, and 41spa) are from slightly brighter areas in the southern part of the basin; and the three marked with small dashes (53spa, 54spa, and 84spa) are from an area north of the basin. *Pieters et al.* [1993] observed the low UV/VIS ratio and weak 1-μm bands in spectra from the basin interior (33spa, 34spa, 35spa, and 36spa) and interpreted this to represent a mafic component (perhaps similar to low-titanium nearside maria) that is mixed with a highland component, such as might be expected for small mare patches, cryptomaria, and/or excavated mafic materials. The spectra from northeast of the basin (53spa, 54spa, and 84spa) were observed to have slightly higher UV/VIS ratios and shallow 1-μm absorption bands that resemble highland soils, and were interpreted by *Pieters et al.* [1993] to represent basin ejecta. Finally, *Pieters et al.* [1993] described the spectra from the southern portion of the

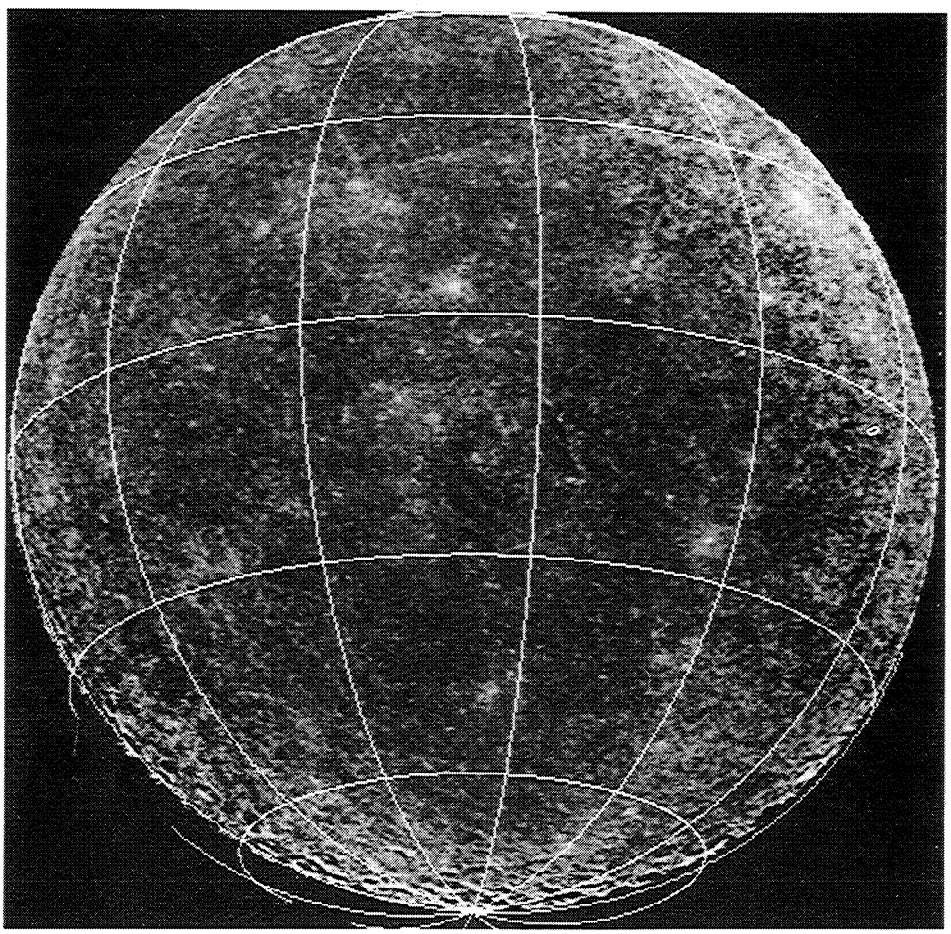

Figure 7a. The 756/990 band ratio or "1-μm band depth" image derived from recalibrated L14 data (compare to Figure 1). The brightest regions, corresponding to fresh mare craters with strong pyroxene absorptions, have the deepest 1-μm absorption bands. Mare soils in Oceanus Procellarum and Mare Humorum have moderately deep mafic mineral absorptions and are moderately bright in this image. The highlands and maria in Mare Grimaldi and Mare Orientale have weak mafic mineral absorptions and are thus dark in this image. By contrast, the Schiller-Schickard cryptomaria and the southeast region of South Pole/Aitken Basin are moderately bright in this image, suggesting moderate 1-μm mafic absorptions.

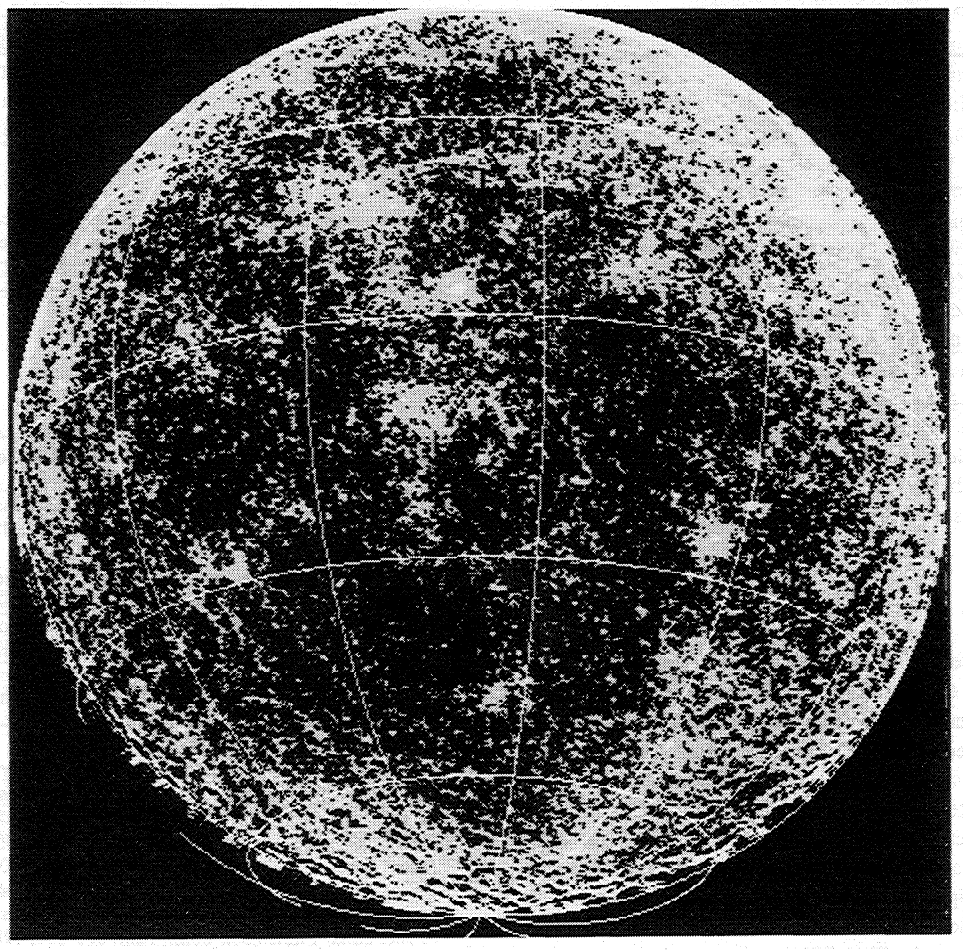

Figure 7b. Contrast-enhanced, density-sliced version of the image shown in Figure 7a, showing the qualitative distribution of the mafic mineral absorptions near Schiller-Schickard and South Pole/Aitken Basin.

basin (39spa, 40spa, and 41spa) as exhibiting moderate albedos, low UV/VIS ratios, and broad, strong 1-μm bands and they interpreted these characteristics as suggestive of the presence of olivine in the southern SPA basin.

The UV/VIS ratios in the recalibrated SPA spectra (Figure 6b) are low (but slightly higher than in the previously calibrated data), so these spectra are still interpretable as representative of low-Ti maria and/or highland contamination. Also note that many of the recalibrated spectra have 1-μm bands of comparable or slightly greater strength than those of the previously calibrated spectra (except for 34spa, which is almost unchanged after recalibration, resembling possibly a low-Ti nearside maria; this spectrum may be in error because it is close to the terminator). Relative reflectance values at 990 nm show decreases of ~3% for 33spa, 35spa, and 53spa; ~2% decreases for 36spa and 84spa; and <1% changes for 39spa, 40spa, 41spa, and 54spa after recalibration. Units with relatively deep 1-μm absorption minima are illustrated qualitatively in Figure 7, where the 756/990 nm ratio image (or "1-μm band depth" image [e.g., *McEwen et al.*, 1993; *Pieters et al.*, 1993]) derived from recalibrated data shows bright areas corresponding to the moderately deep 1-μm minima of the nearside maria, Schiller-Schickard cryptomaria, and south-central, southeastern, and northeastern regions of SPA. Note that the distribution of these mafic-enriched areas corresponds closely with that of *Lucey et al.* [1995], who present a map of the lunar distribution of percent Fe by weight as derived from Clementine data at 750-nm and 950-nm wavelengths.

Many of the recalibrated SPA spectra broadly resemble those of the Schiller-Schickard cryptomaria shown in Figure 5. The three distinct compositional groupings previously observed among the SPA spectra by *Pieters et al.* [1993] are not observed in the recalibrated spectra. Spectra 33spa, 35spa, 36spa, 53spa, 54spa, 84spa, 39spa, 40spa, and 41spa are derived from within the low-albedo region (see Figure 1) that is associated with the area of iron enrichment approximately centered on the SPA basin [*Lucey et al.*, 1995]. All of these spectra exhibit relatively low UV/VIS ratios and moderately strong 1-μm absorption bands suggestive of mare/highland mixed lithologies. The low albedos and relative reflectance characteristics (low UV/VIS, moderately strong 1-μm absorption band) of spectra from the SPA basin interior (33spa, 35spa, and 36spa) support such a mixed lithology. Comparable reflectance characteristics could be produced by mixing a mafic component (perhaps a low-titanium mare deposit) with a highland component, such as might be expected for small mare patches, cryptomaria, and/or excavated mafic materials [as previously described by *Pieters et al.* [1993]). The moderate albedos, low-to-moderate UV/VIS ratios, and moderately strong 1-μm absorption bands of spectra from

northeast of SPA (53spa, 54spa, 84spa) suggest a greater feldspathic component in a mare/highland mixture (54spa and 53spa show positive inflections at 756 μm), as might be expected for a mixture of highland materials and SPA basin ejecta of lower crustal origin. In spectrum 84spa, the high relative reflectance at 556 nm and the broad, strong 1-μm absorption band suggest a larger mafic component (the largest observed in the SPA basin region) in possible basin ejecta deposits of this area. Finally, the moderate albedos, moderate UV/VIS ratios, and strong 1-μm absorption bands (comparable to low-Ti nearside basalts) of recalibrated spectra from the region southeast of SPA (39spa, 40spa, 41spa) support the existence of a mafic component similar to that observed in soils of the Schiller/Schickard cryptomaria. These results suggest that soils of southern SPA may represent basin ejecta with mixed mare and highland spectral signatures; no unusual lithologies are indicated by the recalibrated spectra. The hypothesis that there is an olivine enrichment in the local soils of southern regions of SPA is not strongly supported by spectra shown here.

3. Summary and Conclusion

Updated radiometric calibration and systematic processing procedures for Galileo EM1 SSI data have been described. Application of these updated procedures to L14, a single, whole-disk imaging sequence centered near Mare Orientale, serves primarily to illustrate the effects of the removal of wavelength-dependent scattered light. The removal of scattered light particularly affects the strength of features observed in the 1-μm spectral region and thus has implications for interpretation of mafic mineral signatures in mare deposits on the western lunar limb and farside. A major consequence of the removal of scattered light from the EM1 SSI data is a strengthening of the 1-μm band absorptions of dark areas. Relative reflectance at 990 nm decreases by as much as 10% for the western region of Mare Orientale, but changes of ~5% or less are most common for small maria, cryptomaria, and South Pole/Aitken Basin deposits. Recalibrated spectra from this study indicate that, in conflict with previous results [*Pieters et al.*, 1993; *Greeley et al.*, 1993], small mare ponds of the limb show moderately deep 1-μm absorption bands and thus mafic mineral contents that are comparable to other nearside basalts. The unique lithologies previously proposed for these deposits are not necessary to explain the spectral data. Also, mafic mineral contents of Schiller-Shickard cryptomaria are higher than previously thought [*Pieters et al.*, 1993; *Greeley et al.*, 1993] and are similar to some low-Ti nearside basalts, perhaps in mixture with highland materials. Finally, many of the recalibrated spectra from South Pole/Aitken Basin support the existence of a mafic component similar to that observed in soils of the Schiller/Schickard cryptomaria, suggesting that these soils may represent basin ejecta with mixed mare and highland lithologies. The hypothesis of *Pieters et al.* [1993] that there is an olivine enrichment in the local soils of southern regions of SPA is not supported strongly by spectra shown here.

These results serve to illustrate the importance of adequate scattered-light removal for compositional interpretation of data from Galileo, Clementine, and other future multispectral planetary encounters. Techniques presented here for scattered-light correction do not effectively remove the additional stray light component that originates outside the FOV of the detector. For this study, emphasis on the whole-disk L14 data eliminated the need for distinguishing between scattered light from within and outside the FOV. Proper calibration of data from Galileo and other multispectral imaging missions will require development of additional techniques for the removal of the stray light component.

Acknowledgments. We are grateful to Jim Bell and Scott Murchie for providing very thorough and careful reviews of the original manuscript. Their critical comments helped to strengthen our presentation of this work. This effort was supported by the Galileo SSI Project and NASA Order No. W-18727.

References

Belton, M.J.S., et al., Lunar impact basins and crustal heterogeneity: New western limb and farside data from Galileo, *Science*, *255*, 570-576, 1992.

Cunningham, C., and D. Anthony, Image deconvolution of extended objects: A comparison of the Inverse Fourier and the Lucy techniques, *Icarus*, *102*, 307-315, 1993.

Davies, M.E., T. Colvin, and D.L. Meyer, A unified lunar control network: The near side, *J. Geophys. Res.*, *92*, 14,177-14,184, 1987.

Davies, M.E., T. Colvin, D.L. Meyer, and S. Nelson, The unified lunar control network: 1994 version, *J. Geophys. Res.*, *99*, 23,211-23,214, 1994.

Davis, P.A., Jr., Iron and titanium distribution on the Moon from orbital gamma-ray spectrometry with implications for crustal evolutionary models, *J. Geophys. Res.*, *85*, 3209-3224, 1980.

Davis, P.A., and P. D. Spudis, Global petrologic variations on the Moon: A ternary diagram approach, *Proc. Lunar Planet. Sci. Conf., 17th, Part 2, J. Geophys. Res.*, *92*, suppl., E387-E395, 1987.

Greeley, R., et al., Galileo imaging observations of lunar maria and related deposits, *J. Geophys. Res.*, *98*, 17,183-17,205, 1993.

Hawke, B.R., and J. Bell, Remote sensing studies of lunar dark-halo impact craters: Preliminary results and implications for early volcanism, *Proc. Lunar Planet. Sci. Conf., 12th*, 665-668, 1981.

Head, J.W., S. Murchie, J.F. Mustard, C.M. Pieters, G. Neukum, A. McEwen, R. Greeley, and M.J.S. Belton, Lunar impact basins: New data for the western limb and farside (Orientale and South Pole-Aitken Basins) from the first Galileo flyby, *J. Geophys. Res.*, *98*, 17,149-17,181, 1993.

Helfenstein, P., and J. Veverka, Photometric properties of lunar terrains derived from Hapke's equation, *Icarus*, *72*, 342-357, 1987.

Johnson, J.R., S.M. Larson, and R.B. Singer, Remote sensing of potential lunar resources, 1, Nearside compositional properties, *J. Geophys. Res.*, *96*, 18,861-18,882, 1991.

Klaasen, K., Galileo solid-state imaging subsystem calibration report: Part 2, *JPL Publ. 625-210*, 1993.

Lucey, P.G., G.J. Taylor, and E. Malaret, Abundance and distribution of iron on the Moon, *Science*, *268*, 1150-1153, 1995.

McEwen, A.S., L.R. Gaddis, G. Neukum, H. Hoffmann, C.M. Pieters, and J.W. Head, Galileo observations of post-Imbrian lunar craters during the first Earth-Moon flyby, *J. Geophys. Res.*, *98*, 17,207-17,231, 1993.

Multimission Image Processing Subsystem, Galileo raw experiment data records, CD-ROM, NASA, Jet Propul. Lab., Pasadena, Calif., 1994.

Mustard, J., J. Head, S. Murchie, C. Pieters, M. Belton, and A. McEwen, Schickard cryptomare: Interaction between Orientale ejecta and pre-basin mare from spectral mixture analysis of Galileo SSI data (abstract), *Lunar Planet. Sci., XXIII*, 957-958, 1992.

Pieters, C.M., et al., Crustal diversity of the Moon: Compositional analyses of Galileo SSI data, *J. Geophys. Res.*, *98*, 17,127-17,148, 1993.

Planetary Image Cartography System, *User Manual*, U.S. Geological Survey, Flagstaff, Ariz., 1987.

Pohn, H.A., and R.A. Wildey, A photoelectric-photographic study of the normal albedo of the Moon, *U.S. Geol. Surv. Prof. Pap. Map*, *559-E*, 1970.

Schultz, P.H., and P.D. Spudis, Evidence for ancient mare volcanism, *Proc. Lunar Planet. Sci. Conf., 10th*, 2899-2918, 1979.

Slater, P.N., *Remote Sensing: Optics and Optical Systems*, Addison-Wesley, Reading, Mass., 1980.

Stuart-Alexander, D.E., Geologic map of the central far side of the Moon, *U.S. Geol. Surv. Misc. Inv. Map, I-1147*, scale 1:5,000,000, 1978.

U.S. Geological Survey, Map showing relief and surface markings of the lunar far side, *Map I-1218-A*, scale 1:5,000,000, Flagstaff, Ariz., 1980.

U.S. Geological Survey, Map showing relief and surface markings of the lunar polar regions, *Map I-1326-B*, scale 1:5,000,000, Flagstaff, Ariz., 1981.

U.S. Geological Survey, Map showing relief and surface markings of the lunar near side, *Map I-2276-B*, scale 1:5,000,000, Flagstaff, Ariz., 1992.

Wilhelms, D.E., The geologic history of the Moon, *U.S. Geol. Surv. Prof. Pap., 1348*, 1987.

Wilhelms, D.E., K.A. Howard, and H.G. Wilshire, Geologic map of the south side of the Moon, *U.S. Geol. Surv. Misc. Inv. Map I-1162*, scale 1:5,000,000, 1979.

Zuber, M.T., D.E. Smith, F.G. Lemoine, and G.A. Neumann, The shape and internal structure of the Moon from the Clementine Mission, *Science, 266*, 1839-1843, 1994.

T.L. Becker, L.R. Gaddis, and A.S. McEwen, U.S. Geological Survey, 2255 N. Gemini Drive, Flagstaff, AZ 86001. (e-mail: tbecker@flagmail.wr.usgs.gov; lgaddis@flagmail.wr.usgs.gov; amcewen@flagmail.wr.usgs.gov)

(Received February 21, 1995; revised September 26, 1995; accepted October 4, 1995.)